Applied Thermal Engineering 289 (2026) 129919

Contents lists available at ScienceDirect

Applied Thermal Engineering

journal homepage: www.elsevier.com/locate/apthermeng

Research Paper

Thermally induced structural evolution of diamond surface for pool boiling enhancement

Yunseo Kim [a,b], Daeyoung Kong [c], Jeonghwan Park [a], Bongho Jang [d], Taeyeon Kim [e], Hyuk-Jun Kwon [d], Jungwan Cho [e], Jung Bin In [a,*], Hyoungsoon Lee [a,*]

[a] School of Mechanical Engineering, Chung-Ang University, Seoul 06974, South Korea
[b] School of Mechanical Engineering, University of Maryland, College Park 20740, USA
[c] Department of Mechanical Engineering, Stanford University, Stanford, CA 94305, USA
[d] Department of Electrical Engineering and Computer Science, Daegu Gyeongbuk Institute of Science and Technology (DGIST), Daegu 42988, South Korea
[e] School of Mechanical Engineering, Sungkyunkwan University, 2066 Seobu-ro, Suwon, Gyeonggi-do 16419, South Korea

ARTICLE INFO

Keywords:
Functionalized diamonds
Thermal management
Pool boiling
Power electronics

ABSTRACT

Effective thermal management in power devices is essential for energy-efficient operation. Pool boiling dissipates heat effectively through passive phase changes, eliminating the need for pumping power. However, these benefits remain unrealized in high-power-density devices owing to the risk of reaching Critical Heat Flux (CHF). The superior heat-spreading capabilities of diamond can help mitigate excessive heat flux in such devices. Consequently, pool boiling on diamond surfaces represents a promising cooling strategy for devices with high power densities. However, the inherent chemical inertness of diamond severely limits its surface modification, thereby posing significant challenges to the control of interfacial phenomena. This study investigated methods to modify Polycrystalline Diamond (PCD) surfaces to enhance their pool boiling performance. Thermal oxidation efficiently altered the PCD surface, exploiting its unique material properties. The enhanced surface enabled a 47.8% increase in the heat transfer coefficient and a 119.4% increase in the CHF. Additionally, an in-depth investigation clarified how structural and chemical modifications induced by high-temperature oxidation enhanced pool boiling performance.

1. Introduction

Effective thermal management is essential for the energy-efficient operation of power devices. In particular, regulating the gate junction temperature within a permissible limit is crucial for preventing significant surges in current leakage and thermal stress [1,2]. Therefore, a variety of thermal management techniques have been developed to address these challenges, including mini−/microchannel heat sinks [3,4], jet impingement cooling [5,6], spray cooling [7,8], phase-change materials [9,10], manifold microchannels [11–13], heat pipe [14,15], and evaporative cooling [16]. Two-phase cooling systems are notable for their high energy efficiency and excellent thermal performance. By dissipating heat through phase changes, these systems substantially reduce thermal resistance. In particular, pool boiling systems operate via a passive bubble departure cycle, eliminating the need for pump-powered liquid circulation. Despite these advantages, the application of pool boiling systems in high-heat flux scenarios is limited by their low Critical Heat Flux (CHF).

Dryout refers to the condition in which, under high heat flux, the rate of vapor generation surpasses the incoming liquid supply, causing a shift in the dominant cooling mode from liquid-phase to vapor-phase convection [17,18]. This phenomenon is a primary contributor to the onset of CHF. Notably, the coalescence of vapor bubbles reduces liquid access to the heated surface, thereby hastening dryout. Consequently, strategies to enhance CHF have primarily focused on improving liquid supply and suppressing bubble coalescence [19,20].

Over the past two decades, research has emphasized enhancing surface wettability by modifying both the structure and chemistry of boiling surfaces. For example, Wang and Dhir [21] demonstrated that refining the chemical properties of surfaces enhanced CHF, based on comparisons with smooth surfaces. They compared surfaces with contact angles below 90° and proposed a model to predict CHF by incorporating the effect of wettability through the contact angle.

The most notable progress has been achieved with structured surfaces that promote hemiwicking. A variety of micro-patterns designed to

* Corresponding authors.
E-mail addresses: jbin@cau.ac.kr (J.B. In), leeh@cau.ac.kr (H. Lee).

https://doi.org/10.1016/j.applthermaleng.2026.129919
Received 23 May 2025; Received in revised form 13 October 2025; Accepted 21 January 2026
Available online 26 January 2026

Nomenclature

k	thermal conductivity [W/mK]
q''	heat flux [W/cm^2]
T	temperature [K]
ΔT	wall superheat [K]

Greek symbols

θ	angle [degree]

Subscripts

CA	contact angle
cross	cross-plane
exp	experimental
in	in-plane
max	maximum
sat	saturation

induce capillary action have primarily been fabricated using advanced microfabrication methods. These patterns include micropillars [22,23], microtubes [24], microcavities [24,25], and microchannels [26]. Specifically, Chu et al. [22] achieved a CHF of up to 208 W/cm^2 on a silicon surface with a micropillar structure. They attributed the CHF enhancement on hemiwicking surfaces to contact line pinning beneath the bubble and proposed a model that quantifies this effect through a surface roughness coefficient, defined as the ratio of extended surface area to projected surface area. Further improvements in CHF have been realized with hierarchical structures, wherein nanoscale features are layered onto microstructures. Various nanostructures, including CuO [27,28], SiO_2 [27], nanowires [29,30], ceramics [31], and Cu nanograss [32], have been layered onto microstructures to enhance performance. Rahman et al. [33] reported a CHF of up to 257 W/cm^2 by depositing hierarchical nickel onto micropillars. The volumetric wicking flow rate, a phenomenological parameter representing liquid supply capability, was incorporated into models to predict CHF enhancement from smooth surfaces.

Recently, growing interest has focused on understanding bubble coalescence and exploiting it for boiling enhancement. Most studies have aimed to inhibit bubble coalescence either by patterning regions that promote or suppress nucleation or by modulating thermal conductivity through surface patterning [32,34,35]. For example, Song et al. [32] reported a CHF of up to 256 W/cm^2 on a surface with tube clusters in pillars, where the optimal spacing between nucleation sites ensured sustained liquid supply. In another study, Park et al. [36] demonstrated that the kinetic motion arising from surface energy interactions during bubble coalescence can be exploited to promote early bubble detachment. Additionally, models have been developed to predict CHF by quantifying bubble coalescence through the integration of stochastic behavior [37–39].

Despite these notable advancements, dissipating extreme heat fluxes of several kilowatts from power devices through pool boiling remains fundamentally challenging. Enhanced heat spreading can help pool boiling systems overcome their limitations related to low CHFs. By distributing the extreme heat flux from hotspots, a spreading layer can lower the flux to a few hundred watts per square centimeter at the convective boundary. In this context, diamond is widely recognized for its exceptional heat spreading performance, spurring numerous studies aimed at enhancing thermal performance in electronic devices [40,41].

To optimize cooling performance, strategies combining the efficient phase-change heat transfer at diamond surfaces with the effective heat spreading within diamond layers must be developed. Conventional surface modification techniques for enhancing pool boiling have predominantly relied on Reactive Ion Etching (RIE) of silicon substrates. However, applying such techniques to diamond presents considerable challenges due to its chemical inertness and etch resistance. While silicon can be etched at rates of 10 μm per minute using deep RIE, diamond exhibits substantially lower etch rates, reaching only about 0.08 μm per minute even under ion-assisted sputtering conditions [42,43]. These limitations have markedly restricted the use of diamond as a pool boiling surface. To address this, several researchers have explored alternative processing strategies. Kano [44] employed co-deposition of diamond nanoparticles with nickel to fabricate microstructures, resulting in a CHF of 30 W/cm^2 in fluorinated dielectric fluid. MacNamara et al. [45] reported a CHF of 150 W/cm^2 using Cu–diamond composite coatings deposited via cold spray techniques. Similarly, another team employed metallized diamond combined with sintered nickel, cold-pressed into porous Cu structures, which resulted in a 50% enhancement in Heat Transfer Coefficient (HTC) compared to pure Cu [46]. Torii et al. [47] fabricated micro-diamond-particle-coated surfaces using underwater explosion shock wave techniques, achieving CHF values of approximately 110 W/cm^2.

Notably, pool boiling heat transfer on pristine diamond surfaces remains largely unexplored. Instead, diamond has primarily been employed in composite materials integrated with metals. Most prior studies have instead focused on metal–diamond composite materials, in which the diamond surface is coated with metal and therefore does not directly serve as the phase-change interface. As a result, the fundamental surface properties of diamond in boiling heat transfer have not been adequately investigated. Here, we introduce a thermal oxidation method to fabricate hierarchical structures directly on the diamond surface. This approach aims to enhance the CHF and deliver superior cooling performance by leveraging diamond's exceptional heat-spreading capability. The method provides a straightforward route for diamond surface modification by circumventing its high etching resistance and instead exploiting its inherent crystallographic characteristics. This study systematically examines the surface morphologies generated via thermal oxidation and elucidates the mechanisms responsible for the observed performance enhancement. These findings advance our understanding of diamond's potential as a high-performance pool boiling surface. This research lays the groundwork for future applications in thermal management systems.

2. Experimental method

2.1. Fabrication of pristine diamond surface

PCD was deposited using Chemical Vapor Deposition (CVD). A standard double-side-polished wafer served as the substrate, with nanodiamond particles embedded through ultrasonic seeding. Hydrogen plasma was generated using a 2000 W microwave power source, and pressure was maintained at 50 Torr. Methane gas, supplied as the carbon source at a flow rate of 5 sccm, was directed onto the substrate, which was held at 900 °C to facilitate diamond-phase. Details on the fabrication process for diamond samples are provided in Section I of the Supporting Information. Fig. 1(a)–(f) illustrates a Field Emission Scanning Electron Microscopy (FE-SEM) image and an electron backscatter diffraction map depicting the structural evolution of diamond grains over a 12-h deposition period. Two key growth characteristics influencing the surface structure—lateral grain expansion and re-nucleation are observed. As depicted by the white dashed lines, columnar growth occurs as seed particles grow more rapidly along the out-of-plane direction than along the in-plane direction [48]. With continued planar growth, columns with expanding cross-sections develop. Re-nucleation, caused by defects or dislocations, initiates secondary grain growth from the middle of the film rather than from the seed particles, contributing to random variations in grain orientation and size. Fig. 1(d)–(f) presents top-view images of PCD films deposited over 2, 8, and 12 h, respectively, highlighting the effects of re-nucleation and lateral grain expansion on surface morphology. As the deposition thickness increases, grains

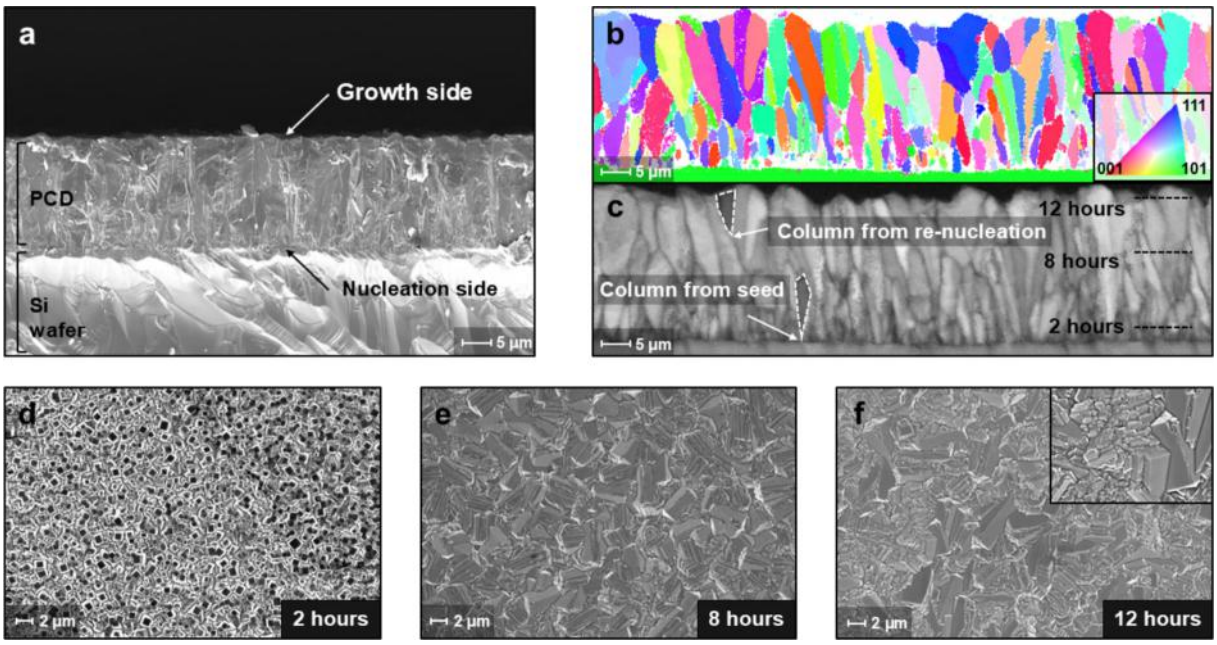

Fig. 1. Structural characteristics of the PCD surface. (a) FE-SEM image, (b) inverse pole figure map, and (c) image quality map captured from the cross-section after 12 h of deposition. Top-view images of the growth surface captured after (d) 2, (e) 8, and (f) 12 h of deposition. As the deposition thickness increases, crystal size expands, and secondary grains become more evident.

enlarge, and longer deposition times result in more active re-nucleation, producing an increased number of small crystallites between larger grains.

2.2. Functionalization of diamond surface

Pristine PCD surfaces typically exhibit low wettability owing to their limited surface areas and low chemical polarity. Enhancing wettability through surface modification is essential for achieving high CHF in water. Notably, thermal oxidation considerably improves wettability by enhancing both the chemical and structural properties of PCD surfaces.

In the thermal oxidation process, amorphous carbon and graphite (sp^2 phase) oxidize and are removed more quickly at lower temperatures than diamond (sp^3 phase) grains [49,50]. This allows selective etching of non-diamond materials at grain boundaries using thermal oxidation at an appropriate temperature. For this process, the furnace was maintained at 660 °C, and 100 sccm of air was supplied as the oxygen source to facilitate etching at the exposed grain boundaries.

Fig. 2(a) schematically presents the morphological evolution induced by high-temperature thermal oxidation. The etching of grain

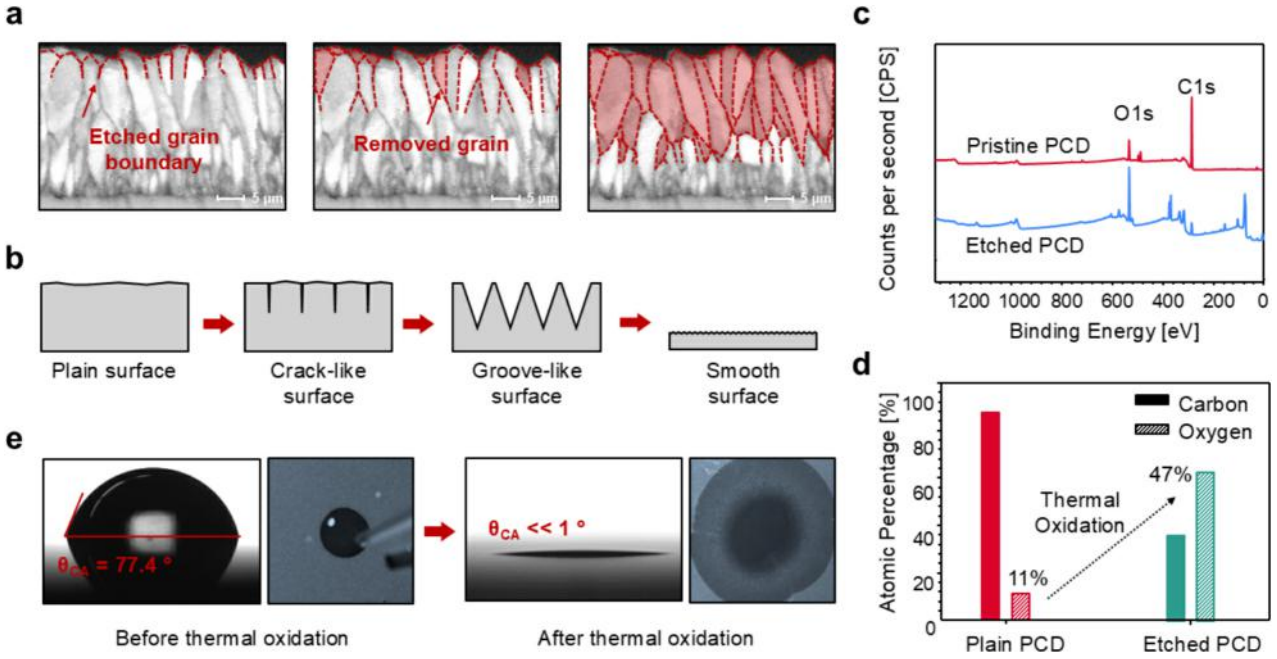

Fig. 2. Surface and chemical composition changes in PCD during thermal oxidation. (a) Removal of grains and grain boundaries, (b) surface structural evolution with increasing etching depth, (c) XPS plot comparison, (d) atomic percentage analysis, and (e) contact angle variations. Thermal oxidation increases surface area and chemical polarity, transforming the less wettable PCD surface into a superhydrophilic surface.

boundaries begins from the exposed top surface, forming narrow gaps between grains, as indicated by the red dashed lines. As these etched boundaries deepen into the substrate, some diamond grains are entirely etched and disappear, marked by the red areas. Depending on the etching depth, this process produces four distinct surface structures, as depicted in Fig. 2(b). For short etching times, the etching depths are shallow, creating crack-like structures at the grain boundaries. With extended etching, re-nucleated grains on the top surface are removed, resulting in a rough surface with micro-grooves. When etching is further prolonged, only nanoscale grains near the substrate remain, producing a relatively smooth surface. Fig. 2(c) and (d) compares the X-ray Photoelectron Spectroscopy (XPS) plots of the PCD surface before and after thermal oxidation to illustrate the changes in its chemical composition. As depicted, oxygen content increases markedly owing to surface oxidation, enhancing surface polarity. This results in a superhydrophilic PCD surface, with a contact angle of less than 1°, as depicted in Fig. 2(e).

In addition to the structural changes caused by varying etching depths, the grain size on the etched surface also influences the surface morphology after thermal oxidation. The grain size on the growth surface begins at approximately 200 nm and progressively increases, exceeding 5 μm in cross-sectional diameter after 12 h. As the grain size increases, larger fins form during thermal oxidation, resulting in more pronounced hierarchical morphologies in samples with larger grains. To create diverse surface structures, six PCD surfaces with three distinct grain sizes were fabricated by etching over different durations. Table 1 summarizes the fabrication parameters and corresponding surface properties of the resulting PCD samples. Notably, samples labeled with "E-" indicate those etched via thermal oxidation, while samples prefixed with "B-" denote pristine samples without modification. As illustrated in the FE-SEM images displayed in Fig. 3(a)–(e), samples E-PCD1, E-PCD3, and E-PCD4 were etched to relatively shallow depths, producing crack-like structures. As depicted by the top-view images, a considerable portion of the top surface remains unetched. Small-grain samples subjected to extended etching times develop smooth surfaces owing to the excessive removal of crystal layers. Notably, sample E-PCD5 was subjected to a longer etching process than sample E-PCD4, leading to greater removal of crystallites from the top surface and the formation of a groove-like structure. Consequently, the surface morphology gradually shifts from crack-like to predominantly groove-like features.

The surface roughness coefficients, defined as the ratio of total surface area to projected surface area, were measured using a 3D confocal microscope (OLS4100-SWF, Olympus Co., Ltd., Japan). These measurements reflect the enhancement in surface area resulting from the formation of fin structures. These measurements were performed over a 645 × 645 μm^2 area with a resolution of 10 nm. A notable increase in surface area is observed for samples with deeply etched large grains. The contact angle was measured using a droplet shape analyzer (SmartDrop, Femtobiomed, Korea) equipped with free surface goniometry and gravity effect modulation algorithms. Droplets with a volume of 5 μL were dispensed, and measurements were conducted at five different locations on each sample. With the exception of the E-PCD2 sample, which had a smooth surface due to excessive etching, the remaining samples exhibited strong wicking behavior. Because the deposited droplets were rapidly absorbed into the porous structure, the apparent contact angles were below the measurable limit and were recorded as less than 1°.

2.3. Test procedure and uncertainties

Fig. 4 presents the configuration of the pool boiling experimental setup. To evaluate the heat transfer performance, a 200 nm-thick Au thin-film heater with a 20 nm Ti adhesion layer was deposited via thermal evaporation to provide uniform heat flux over a 1 × 1 cm^2 area through Joule heating. A 500-nm-thick SiO_2 insulation layer was deposited using plasma-enhanced CVD. The heater was designed in a serpentine shape to achieve resistance between 155.1 Ω and 194.8 Ω. The samples were sealed in a Polyetherketone (PEEK) plate with silicon adhesive (*DOWSIL*, RTV 3145) and bolted into an aluminum chamber with a 7 L capacity. Before the experiment, deionized water was preheated in an electric kettle and added to the chamber. An immersion heater positioned at the same height as the PEEK fixture was then used to boil and degas the water within the chamber. A reflux condenser on the ceiling, supplied with cold water from a chiller (*Jeiotech*, HH20), condensed the vaporized working fluid, allowing it to return to the liquid pool. To maintain a near-saturation state during the experiment, a K-type thermocouple (*Omega*, KMQSS-062G-6) and an absolute gauge pressure transducer (*TRAFAG E*, CT8472) were installed at the same height as the boiling surface and monitored using a data acquisition module (*National Instruments*, NI-9214/NI-9220). Heating power for the heater was supplied by a DC power source (*HP*, 6030A), and a custom voltage divider was used to control the heat flux applied to the heating surface. This divider consisted of two high-resistance resistors (39 kΩ and 1 kΩ) for voltage sensing and a low-resistance shunt resistor (0.05 Ω ± 0.5%) for current sensing. The voltage across the 1 kΩ resistor and the shunt resistor was measured at 1 kHz using a data acquisition system and a voltage module (*National Instruments*, NI 9220). The resulting measurement data were then used to calculate the total power and estimate the heat flux by dividing by the heating surface area. The temperature distribution of the heater surface was captured using an IR thermal imaging camera (*FLIR*, A655sc) with a resolution of 640 × 480 pixels. A thin layer of black paint with an emissivity of 0.94 (*ELE*, EP-10) was applied to the heater surface. A high-speed camera (*Photron*, FASTCAM Mini UX100) was used to optically capture bubble dynamics at a resolution of 1280 × 1024 pixels and a frequency of 2000 fps. The propagation of uncertainty was calculated, yielding maximum errors of 1.81% for temperature and 0.49% for heat flux. Details of component-level measurement uncertainties, graphs with error bars, and repeatability test results are provided in Fig. S2 of the Supporting Information. The propagation of uncertainty in the experimental measurements was evaluated using the root-sum-of-squares method, which combines the uncertainties of the acquired values. Heat flux was calculated using Eq. (1), which incorporates uncertainties in the voltage divider resistance and voltage module measurements. The maximum error in the heat flux calculation was determined to be ±0.49%.

$$\left(\frac{U_{q_{heater}}}{VI}\right)^2 = \left(\frac{U_{V_{heater}}}{V_{heater}}\right)^2 + \left(\frac{U_{I_{heater}}}{I_{heater}}\right)^2 \quad (1)$$

Rapid bubble formation and departure cause pronounced fluctuations in wall temperature. Steady state was defined as the condition

Table 1
Design parameters and surface characteristics of the fabricated PCD samples.

Number	Sample	Deposition time [h]	Etching time [min]	Total thickness [μm]	Base thickness [μm]	Surface roughness coefficient	Contact angle [°]
1	B-PCD	2	0	3.8	3.8	1.202	77.4
2	E-PCD1	2	2	3.4	2.5	1.204	~1
3	E-PCD2	2	5	1.1	1.1	1.088	11.2
4	E-PCD3	8	10	11.3	9.6	1.488	~1
5	E-PCD4	12	30	25.3	15.2	3.223	~1
6	E-PCD5	12	50	20.2	11.4	2.672	~1

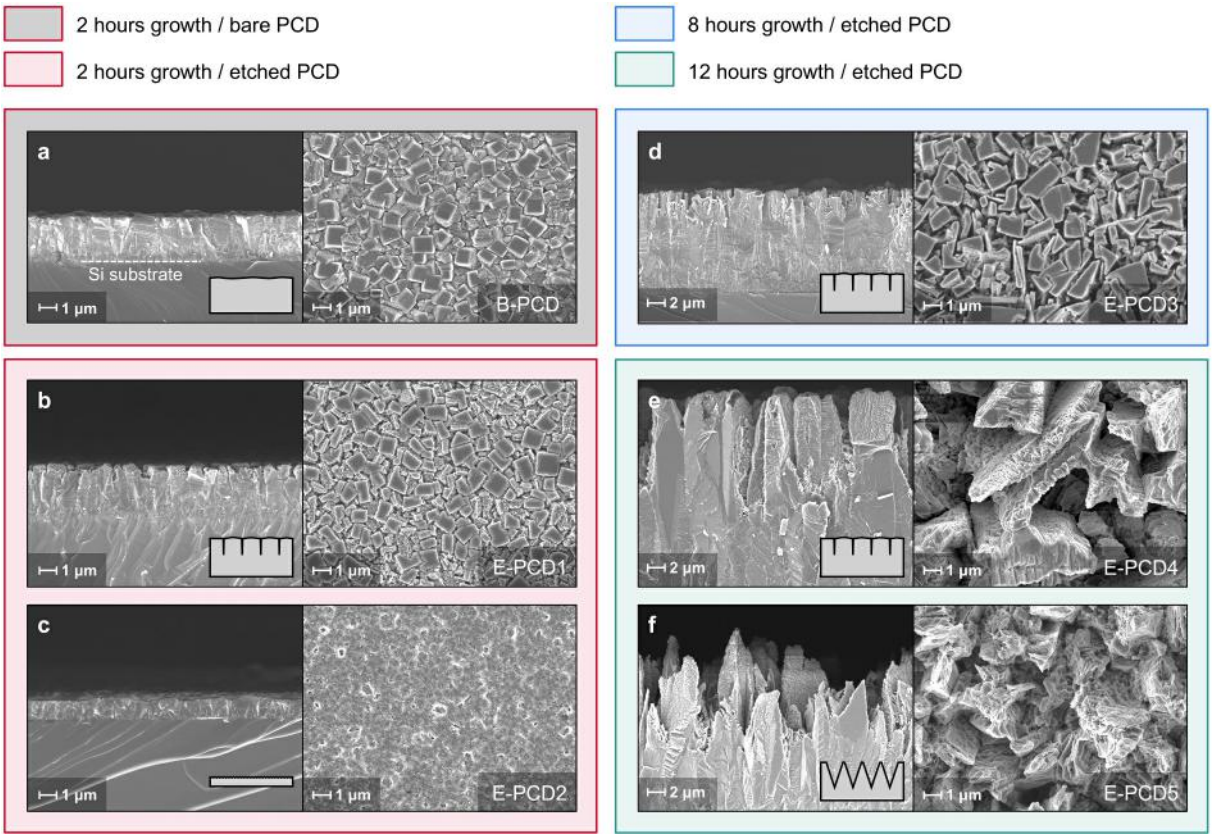

Fig. 3. FE-SEM images of the surfaces of the fabricated PCD samples: (a) B-PCD, (b) E-PCD1, (c) E-PCD2, (d) E-PCD3, (e) E-PCD4, and (f) E-PCD5.

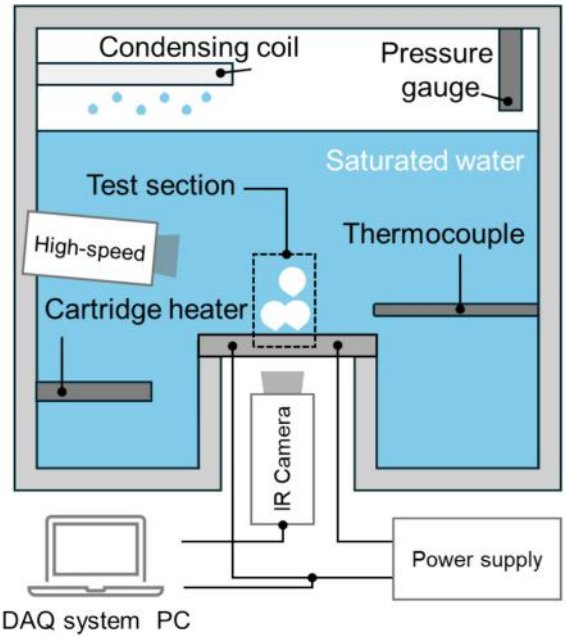

Fig. 4. Schematic view of the pool boiling experimental setup.

where average temperature fluctuations remained within 0.1 °C over a 10 s interval. After reaching steady state, the average temperature of the heating area was recorded over 30 s, with a relative error of up to 0.39%. The boiling surface temperature was then calculated using Fourier's law, based on the time-averaged heater temperature across the heating area. To account for the temperature-dependent thermal conductivity of the silicon substrate, a finite difference discretization scheme with 5 μm intervals was used. The HTC was obtained by dividing the heat flux by the difference between the average surface temperature and the saturation temperature of water (100 °C). HTC uncertainty was evaluated using the following equation, resulting in a relative error of up to 18.68%.

$$\left(\frac{U_{HTC}}{HTC}\right)^2 = \left(\frac{U_{V_{heater}}}{V_{heater}}\right)^2 + \left(\frac{U_{I_{heater}}}{I_{heater}}\right)^2 + \left(\frac{U_{\Delta T_s}}{\Delta T_s}\right)^2 \quad (2)$$

3. Results and discussion

3.1. Intrinsic pool boiling characteristics of the PCD surface

Fig. 5(a) illustrates the pool boiling performance of the pristine PCD surface, highlighting the influence of its inherent chemical surface properties by comparing it with the polished surfaces of Cu [51], Al [51], SUS [51], and SiO_2 [22]. Fig. 5(b) presents the relationship between apparent contact angle and CHF. Given that most surfaces are polished, the apparent contact angle can be considered equivalent to the intrinsic contact angle, which is defined as the contact angle determined solely by the chemical composition on a perfectly smooth surface. All samples exhibit moderate hydrophilicity, which does not induce wicking. The PCD surface fabricated in this study displays a large contact angle of 77°; meanwhile, the other metallic surfaces present smaller contact angles, ranging from 12° to 65°, depending on their degree of polishing and oxidation. Owing to the inherent poor wettability of the PCD surface, it demonstrates a noticeably lower CHF than the other material surfaces. The CHF data for these materials, except for the extremely well-polished smooth SiO_2 surface, closely align with the predictions of Kandlikar's CHF model [52], which incorporates wettability characterization. Wall superheat, strongly influenced by the number of nucleation sites, is relatively lower on the PCD surface

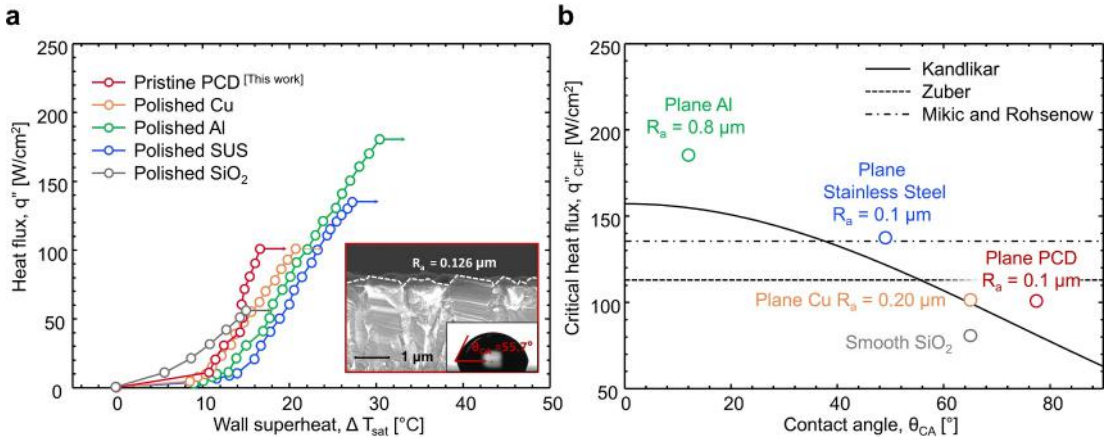

Fig. 5. Comparison of the pool boiling characteristics of the PCD surface with those of Cu [51], Al [51], SUS [51], and SiO_2 [22] Surfaces. (a) Heat flux vs. wall superheat plot and (b) CHF vs. contact angle plot with model predictions [52–54]. Owing to its large intrinsic contact angle, the PCD surface has a relatively low CHF but benefits from a lower wall superheat. Shallow surface features on the growth surface create spaces for gas entrapment.

compared to the other material surfaces. As illustrated in the inset of Fig. 5(a), misaligned grains on the PCD surface create spaces for gas entrapment. Although these spaces are too shallow to substantially improve wettability, they can effectively promote incomplete wetting, particularly leveraging the large intrinsic contact angle of PCD. The reduced energy barrier for nucleation at these gas-trapping sites likely contributes to the decrease in wall superheat.

3.2. Enhanced pool boiling heat transfer on a modified PCD surface

This section examines how thermal oxidation–induced structural and chemical changes of diamond surfaces contribute to reducing wall superheat and enhancing CHF. Fig. 6 illustrate the enhanced pool boiling performance of the PCD surface after thermal oxidation. Fig. 6(a) compares the boiling curves of three crack-like structures to illustrate the effect of grain size on boiling performance enhancement. Etched

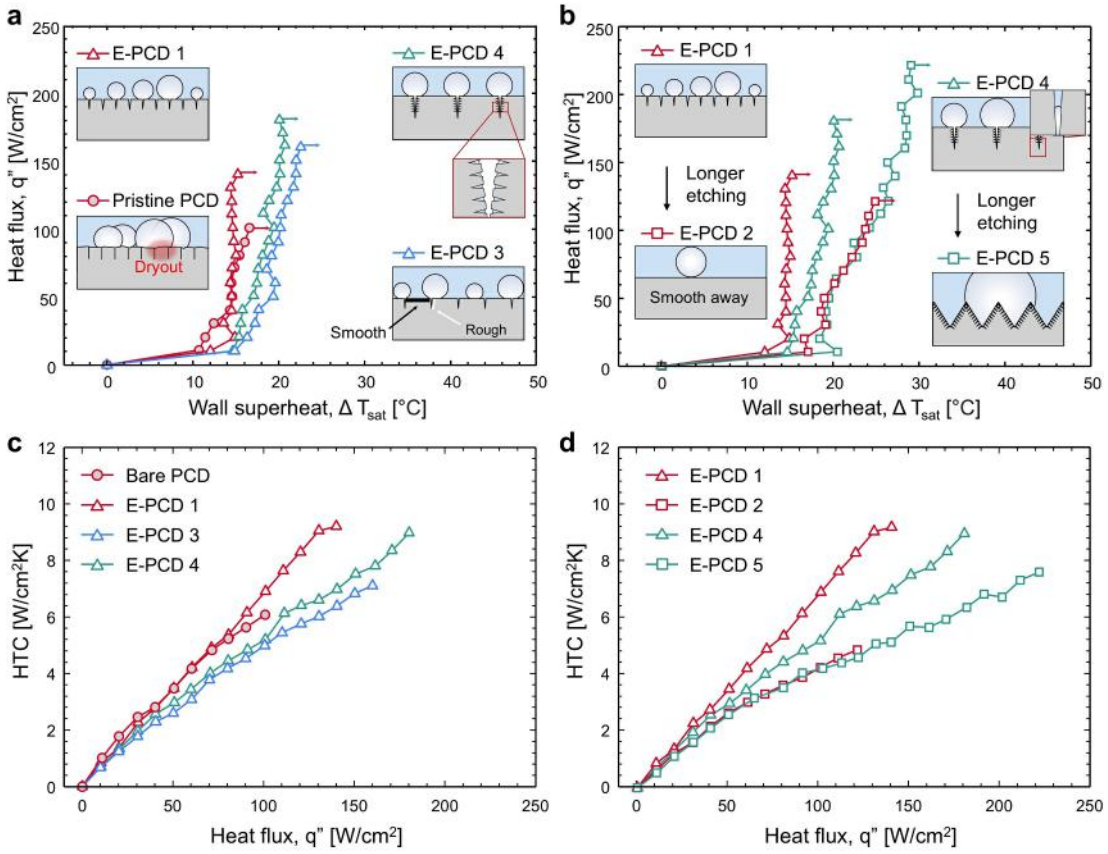

Fig. 6. Enhancement of pool boiling performance on etched diamond surfaces: (a, c) Comparisons of crack-like structures with varying grain sizes: heat flux vs. wall superheat and HTC vs. heat flux. (b, d) Comparisons of surfaces with varying structural types: heat flux vs. wall superheat and HTC vs. heat flux. The inset in (a) illustrates that as the grain boundaries are etched into cracks, smaller grain sizes result in higher nucleation site density. It further demonstrates that micro-layer evaporation is enhanced on the walls of the etched cracks. The inset in (b) indicates that the crack-like structure exhibits a narrow angle, while the groove structures display a wider angle. Specifically, the narrow-angled crack-like structure facilitates gas entrapment, thereby increasing the nucleation site density.

PCD surfaces with crack-like structures exhibit an Onset of Nucleate Boiling (ONB) temperature that is 5 °C higher than that of the bare PCD surface. This increase in the ONB temperature is attributed to increased polarity, which reduces the intrinsic contact angle, making gas entrapment in wide-angle cavities less favorable. Differences in wall superheat among the three crack-like structures are linked to their surface morphology. These surfaces exhibit varying crack densities, as the grain boundaries evolve into cracks during thermal oxidation. These cracks form narrow-angled spaces that trap gas and serve as nucleation sites; thus, a higher crack density effectively reduces wall superheat. Consequently, among all the tested samples, E-PCD1 exhibits the lowest wall superheat owing to its notably small grain size and highest crack density.

The nano/microscale hierarchical roughness of the etched wall further lowers wall superheat by establishing a three-phase contact line that enhances micro-layer evaporation, as depicted in the enlarged red box on the schematic of E-PCD4 in Fig. 6(a). The impact of micro-layer evaporation can be examined by comparing samples E-PCD3 and E-PCD4, both of which exhibit a similarly low number of nucleation sites owing to their large grain size. As illustrated in Fig. 3, the top surfaces of the grains remain relatively smooth, while the crack walls exhibit increased roughness due to cleavage of carbon–carbon bonds induced by interactions with oxygen atoms. Sample E-PCD4 is deeply etched along the large grains, resulting in excessive nano-hierarchical structures, whereas E-PCD3, with shallower etching, retains smoother top surfaces. Fig. 6(b) illustrates the changes in pool boiling performance with increasing etching depth, which results in the formation of groove-like structures and smooth surfaces. Owing to its longer thermal oxidation process compared to E-PCD1, E-PCD2 experienced excessive grain removal, resulting in a smooth surface. As the pores capable of trapping bubbles were eliminated, nucleation was notably suppressed, resulting in increased wall superheat. E-PCD5, which underwent a longer thermal oxidation process than E-PCD4, developed groove-like structures as the small grains on its surface were removed. Notably, groove-like structures exhibit higher superheat and CHF than crack-like structures. E-PCD5 exhibits a superheat level similar to that of the smooth E-PCD2, suggesting that the nucleation enhancement enabled by incomplete wetting has nearly vanished.

Fig. 7(a)–(d) presents IR thermographic images of the heater surfaces and high-speed photographic views of the boiling surfaces of E-PCD4 and E-PCD5 at a heat flux of 30 W/cm^2. These images elucidate the influence of nucleation site density on bubble departure dynamics and wall temperature. From the temperature distributions shown in the IR thermographic images in Fig. 7(a) and (c), active nucleation sites can be identified by their lower temperatures. E-PCD4 exhibits a higher nucleation site density than E-PCD5 because its narrow-angled crack structures facilitate gas entrapment, while the wide-angled grooves in E-PCD5 are less conducive to this effect. The high-speed camera images in Fig. 7(b) and (d) indicate that the nucleation site density also plays a key role in bubble departure frequency. The dense nucleation sites on E-PCD4 promote frequent bubble coalescence, resulting in earlier detachment [36]. In contrast, bubbles on E-PCD5 grow with minimal interference until sufficient buoyancy is achieved, leading to detachment at larger sizes and over longer durations. By comparing the wall temperatures beneath the bubble, marked by white dashed lines in Fig. 7 (a) and (c), evaporation is found to be more effectively enhanced on E-PCD5. This observation suggests that the groove-like structures develops the most abundant nanostructures among the tested structures, contributing to a larger thin-film area. Despite the lowest wall superheat being observed beneath the bubble, the surrounding single-phase regions remain at high wall superheat. As a result, E-PCD4, which has a larger number of nucleation sites, exhibits a lower average wall superheat, as shown in Fig. 6.

Fig. 8(a)-(d) illustrates how bubble coalescence contributes to the triggering of CHF, based on bubble dynamics at 190 W/cm^2, a condition that induces rapid bubble generation. Owing to its high nucleation site density, the crack-like structure of E-PCD4 promotes early bubble coalescence, leading to the formation of a large bubble. The resulting bubble behavior, as observed in the IR image, initiates a large central dry spot that expands rapidly. In contrast, the lower nucleation site density of E-PCD5 results in partial bubble coalescence and the formation of three distinct clusters; this configuration preserves liquid supply paths and effectively suppresses dry spot expansion.

Fig. 9(a)–(b) illustrates structural factors contributing to CHF enhancement on modified PCD surfaces. Samples with larger grains presented greater CHF improvement compared to those with smaller grains, with E-PCD5 achieving up to a 119.4% increase over the bare PCD surface. On superhydrophilic surfaces, where liquid spreading is prominent, the liquid supply to dry patches cannot be entirely

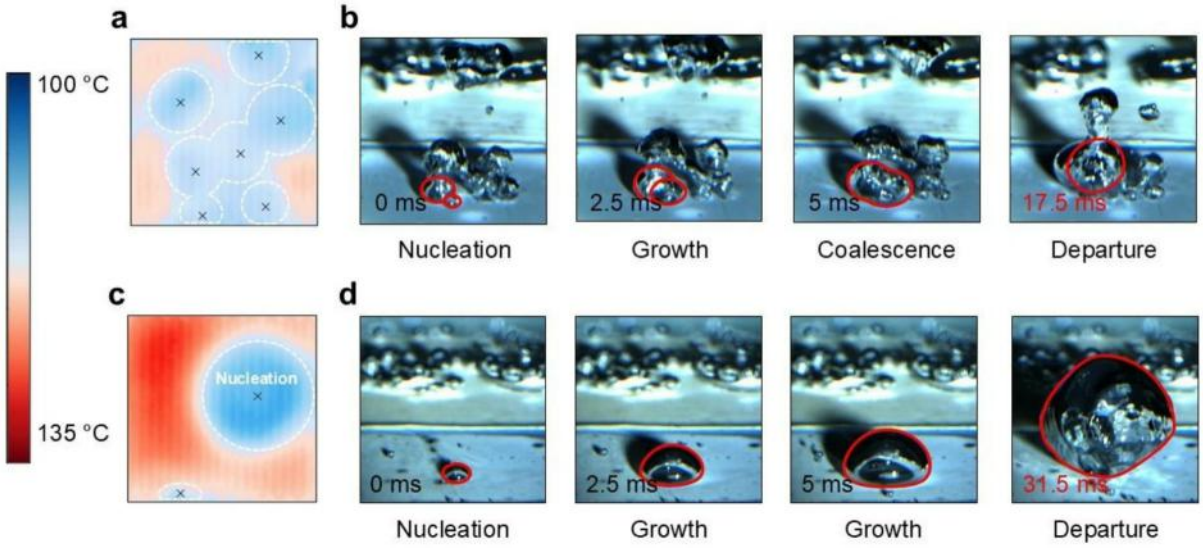

Fig. 7. IR thermographic images of the heater surfaces of (a) E-PCD4 and (c) E-PCD5 and high-speed image sequences of the boiling surfaces of (b) E-PCD4 and (d) E-PCD5 at a heat flux of 30 W/cm^2. In the IR thermographic images, the white dashed regions indicate areas of active nucleation where phase change occurs. In the high-speed images, the red dashed lines highlight the expanding boundary of the growing bubble. Multiple bubbles grow simultaneously on the crack-like structures of E-PCD4, indicating a high nucleation site density, whereas the groove-like structure of E-PCD5 exhibits the formation of a single bubble. In (b), two adjacent bubbles coalesce during growth and detach at an early stage.

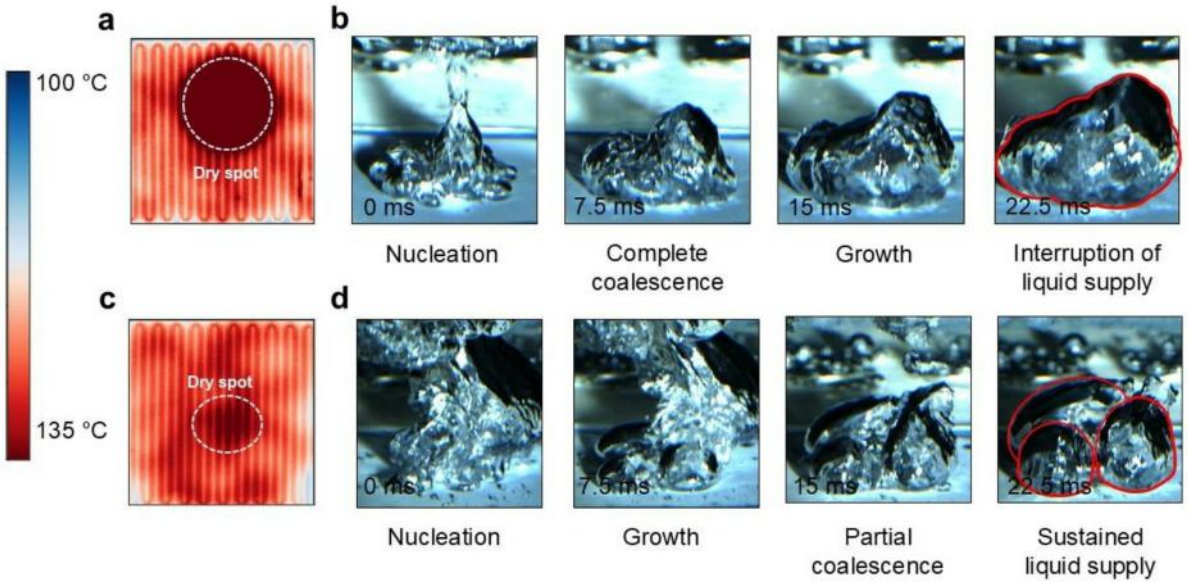

Fig. 8. IR thermographic images of the heater surfaces of (a) E-PCD4 and (c) E-PCD5 and high-speed image sequences of the boiling surfaces of (b) E-PCD4 and (d) E-PCD5 at a heat flux of 190 W/cm^2. The red dashed lines in the high-speed images delineate the boundaries of the coalesced bubbles. In the crack-like structure, bubbles grow in a fully coalesced state, thereby interrupting liquid supply. In contrast, the groove-like structure exhibits partial coalescence while maintaining liquid supply paths toward the center of the boiling surface. The white dashed lines in the IR images denote the dry spots. As the vaporization rate becomes comparable to the liquid supply rate toward the center, repeated formation and disappearance of dry spots are observed.

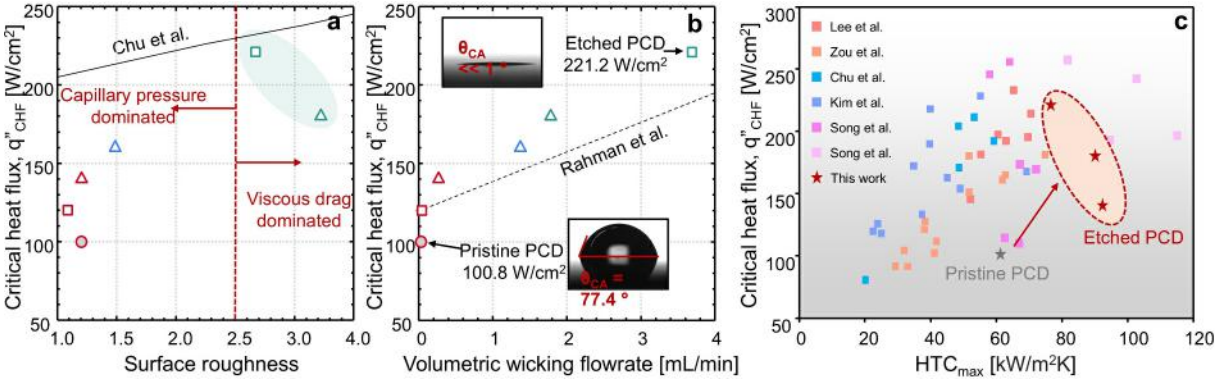

Fig. 9. Comparison between experimental and predicted CHF values: (a) as a function of surface roughness coefficient [22] and (b) as a function of volumetric wicking flow rate [33]. The dashed lines represent the CHF values predicted by the models, and the symbols correspond to the experimental data. (c) concluding remarks [22–24,28,32,55].

characterized by contact angle alone.

Fig. 9(a) compares the experimental CHF values with those predicted using the surface roughness coefficient proposed by Chu et al. [22]. Although the model predicts that CHF increases with increasing surface roughness, the experimental results for E-PCD4 and E-PCD5 (indicated in green) exhibit the opposite trend. This deviation arises from the restricted liquid replenishment observed in excessively miniaturized structures. When the surface area enhancement surpasses a critical threshold, viscous drag outweighs the benefits of increased capillary pressure, thereby limiting the overall liquid supply.

Fig. 9(b) compares the experimental CHF values with those predicted using the model introduced by Rahman et al. [33]. The volumetric wicking flow rate was calculated using the approach described by Kim et al. [23], which incorporates both capillary forces and viscous drag. Despite exhibiting a greater surface area, E-PCD4 demonstrates a lower wicking velocity than E-PCD5. This suggests that the cracks formed during thermal oxidation are intrinsically too narrow, resulting in substantial viscous resistance. Consequently, liquid flows more readily through the wider grooves of E-PCD5.

Fig. 9(c) presents a comparison of the CHF and HTC measured on the enhanced diamond surface with values reported in previous studies. The crack-like and groove-like structures exhibit higher CHF and HTC than micro-patterned surfaces fabricated through DRIE-based processes. This finding demonstrates that the challenges associated with diamond machining can be addressed and that surface enhancement is achievable without reliance on mask-based processes. While previous studies typically relied on a two-step process—etching microstructures followed by nanostructure deposition—to achieve hierarchical architectures, our approach provides a manufacturing advantage by enabling their formation in a single thermal oxidation step. In addition, the results presented here capture only the improvement in convective heat transfer, excluding the effects of heat spreading. In practical high-power devices with tiny heat sources and extreme heat fluxes, the superior heat spreading capability of diamond is expected to play a dominant role, substantially amplifying its overall cooling performance.

4. Conclusions

This study investigated the intrinsic pool boiling properties of diamond surfaces and introduced a surface enhancement method for energy-efficient cooling of high-power devices. Notably, given the non-polar nature and low surface energy of PCD, its surface exhibited poor wettability, constraining the CHF to 100 W/cm^2. However, high-temperature oxidation substantially improved the wettability of the diamond surface, increasing the CHF to as high as 220 W/cm^2. Three distinct surface morphologies were apparent, depending on the depth of the etched grain boundaries. Among these, groove-like structures yielded the greatest CHF enhancement, with an increase of 119.4%. Their large surface area and optimal gap spacing notably increased wicking velocity. However, the induced chemical polarity weakened nucleation activity, thereby increasing wall superheat. Crack-like structures counteracted this effect by promoting incomplete wetting, leading to a 47.8% increase in the maximum heat transfer coefficient. Excessive grain removal produced an overly smooth surface, eliminating structural features and leaving only chemical modifications. On smooth hydrophilic surfaces, CHF improvement was severely limited and nucleation was strongly suppressed, underscoring the importance of incorporating structural modifications. Integrating these pool boiling enhancements with the superior heat-spreading properties of diamond could enable energy-efficient cooling solutions for high-heat-flux devices.

CRediT authorship contribution statement

Yunseo Kim: Writing – original draft, Visualization, Validation, Resources, Project administration, Methodology, Investigation, Formal analysis, Data curation, Conceptualization. **Daeyoung Kong:** Methodology. **Jeonghwan Park:** Writing – review & editing, Investigation. **Bongho Jang:** Methodology. **Taeyeon Kim:** Supervision, Methodology. **Hyuk-Jun Kwon:** Methodology. **Jungwan Cho:** Supervision, Methodology. **Jung Bin In:** Writing – review & editing, Supervision, Methodology, Funding acquisition. **Hyoungsoon Lee:** Writing – review & editing, Supervision, Methodology, Funding acquisition.

Funding sources

This work was supported by the National Research Foundation of Korea(NRF) grant funded by the Korea government(MIST) (No. RS-2024-00411577, No. RS-2024-00353227), and the Chung-Ang University Graduate Research Scholarship in 2024.

Declaration of competing interest

The authors declare that they have no known competing financial interests or personal relationships that could have appeared to influence the work reported in this paper.

Appendix A. Supplementary data

Supplementary data to this article can be found online at https://doi.org/10.1016/j.applthermaleng.2026.129919.

Data availability

Data will be made available on request.

References

[1] H. Su, F. Liu, A. Devgan, E. Acar, S. Nassif, Full chip leakage estimation considering power supply and temperature variations, in: Proceedings of the 2003 International Symposium on Low Power Electronics and Design, Association for Computing Machinery, New York, NY, USA, 2003, pp. 78–83, https://doi.org/10.1145/871506.871529.

[2] R. Khazaka, L. Mendizabal, D. Henry, R. Hanna, Survey of high-temperature reliability of power electronics packaging components, IEEE Trans. Power Electron. 30 (2015) 2456–2464, https://doi.org/10.1109/TPEL.2014.2357836.

[3] S.V. Garimella, V. Singhal, D. Liu, On-Chip thermal management with microchannel heat sinks and integrated micropumps, Proc. IEEE 94 (2006) 1534–1548, https://doi.org/10.1109/JPROC.2006.879801.

[4] A. Ateş, S. Çelik, V. Yağcı, M.Ç. Malyemez, M. Parlak, A.K. Sadaghiani, A. Koşar, Flow boiling of dielectric fluid HFE–7000 in a minichannel with pin fin structured surfaces, Appl. Therm. Eng. 223 (2023) 120045.

[5] N. Zuckerman, N. Lior, J.P. Hartnett, A. Bar-Cohen, Y.I. Cho, Jet impingement heat transfer: Physics, correlations, and numerical Modeling, in: G.A. Greene (Ed.), Advances in Heat Transfer, Elsevier, 2006, pp. 565–631, https://doi.org/10.1016/S0065-2717(06)39006-5.

[6] S.V. Ekkad, P. Singh, A modern review on jet impingement heat transfer methods, J. Heat Transf. 143 (2021), https://doi.org/10.1115/1.4049496.

[7] J. Kim, Spray cooling heat transfer: the state of the art, Int. J. Heat Fluid Flow 28 (2007) 753–767, https://doi.org/10.1016/j.ijheatfluidflow.2006.09.003.

[8] Y. Kim, S. Jung, S. Kim, S.T. Choi, M. Kim, H. Lee, Heat transfer performance of water-based electrospray cooling, Int. Commun. Heat Mass Transf. 118 (2020) 104861, https://doi.org/10.1016/j.icheatmasstransfer.2020.104861.

[9] A.M. Randriambololona, V. Manepalli, R.C. McAfee, B. Ojha, R. Miraftab-Salo, K. Guye, H. Lee, S. Graham, D. Agonafer, Three-component composite phase change material (PCM) for electronics subject to transient/pulsed heat loads, IEEE Trans. Compon. Packag. Manuf. Technol. 14 (2024) 2248–2257.

[10] V.V. Manepalli, R.C. McAfee, A.M. Randriambololona, S. Graham, D. Agonafer, Dynamic thermal management of a MOSFET power module using a novel three-component phase change material, ASME J. Heat Mass Transf. 147 (2025) 102401.

[11] D. Kong, Y. Kim, M. Kang, E. Song, Y. Hong, H.S. Kim, K.J. Rah, H.G. Choi, D. Agonafer, H. Lee, A holistic approach to thermal-hydraulic design of 3D manifold microchannel heat sinks for energy-efficient cooling, Case Stud. Therm. Eng. 28 (2021) 101583, https://doi.org/10.1016/j.csite.2021.101583.

[12] K. Kim, D. Kong, Y. Kim, B. Jang, J. Cho, H.-J. Kwon, H. Lee, Enhanced boiling heat transfer via microporous copper surface integration in a manifold microgap, Appl. Therm. Eng. 241 (2024) 122325, https://doi.org/10.1016/j.applthermaleng.2023.122325.

[13] Y. Kim, D. Kong, R.D. Selvakumar, M. Kang, N. Kang, J. Kwon, H. Lee, Thermal-hydraulic characterization in manifold-microchannel heat sinks for energy-efficient cooling of HEV/EV power modules, Appl. Therm. Eng. 265 (2025) 125611, https://doi.org/10.1016/j.applthermaleng.2025.125611.

[14] R. Wrobel, R.J. Mglen, Heat pipes in thermal management of electrical machines – a review, Therm. Sci. Eng. Progr. 26 (2021) 101053, https://doi.org/10.1016/j.tsep.2021.101053.

[15] S. Lee, S. Kang, Y. Kim, G. Geum, D. Kong, D.H. Shin, S.H. Lee, J. Lee, H. Lee, Thermal design framework of heat pipe heat exchanger for efficient waste heat recovery, Energy 318 (2025) 134731, https://doi.org/10.1016/j.energy.2025.134731.

[16] K. Guye, D. Dong, Y. Kim, H. Lee, B. Dogruoz, D. Agonafer, Guidelines for designing micropillar structures for enhanced evaporative heat transfer, J. Electron. Packag. 143 (2021) 041106.

[17] T.G. Theofanous, T.N. Dinh, J.P. Tu, A.T. Dinh, The boiling crisis phenomenon: part II: dryout dynamics and burnout, Exp. Thermal Fluid Sci. 26 (2002) 793–810, https://doi.org/10.1016/S0894-1777(02)00193-0.

[18] N.S. Dhillon, J. Buongiorno, K.K. Varanasi, Critical heat flux maxima during boiling crisis on textured surfaces, Nat. Commun. 6 (2015) 8247, https://doi.org/10.1038/ncomms9247.H.J. Cho, D.J. Preston, Y. Zhu, E.N. Wang, Nanoengineered materials for liquid–vapour phase-change heat transfer, Nat Rev Mater 2 (2016) 1–17. Doi: 10.1038/natrevmats.2016.92.

[19] G. Liang, I. Mudawar, Review of pool boiling enhancement by surface modification, Int. J. Heat Mass Transf. 128 (2019) 892–933, https://doi.org/10.1016/j.ijheatmasstransfer.2018.09.026.

[20] H.J. Cho, D.J. Preston, Y. Zhu, E.N. Wang, Nanoengineered materials for liquid–vapour phase-change heat transfer, Nat. Rev. Mater. 2 (2016) 1–17, https://doi.org/10.1038/natrevmats.2016.92.

[21] C.H. Wang, V.K. Dhir, Effect of surface wettability on active nucleation site density during Pool boiling of water on a vertical surface, J. Heat Transf. 115 (1993) 659–669, https://doi.org/10.1115/1.2910737.

[22] K.-H. Chu, R. Enright, E.N. Wang, Structured surfaces for enhanced pool boiling heat transfer, Appl. Phys. Lett. 100 (2012) 241603, https://doi.org/10.1063/1.4724190.

[23] S.H. Kim, G.C. Lee, J.Y. Kang, K. Moriyama, M.H. Kim, H.S. Park, Boiling heat transfer and critical heat flux evaluation of the pool boiling on micro structured surface, Int. J. Heat Mass Transf. 91 (2015) 1140–1147, https://doi.org/10.1016/j.ijheatmasstransfer.2015.07.120.

[24] Y. Song, S. Gong, G. Vaartstra, E.N. Wang, Microtube surfaces for the simultaneous enhancement of efficiency and critical heat flux during Pool boiling, ACS Appl. Mater. Interfaces 13 (2021) 12629–12635, https://doi.org/10.1021/acsami.1c00750.

[25] D.E. Kim, S.C. Park, D.I. Yu, M.H. Kim, H.S. Ahn, Enhanced critical heat flux by capillary driven liquid flow on the well-designed surface, Appl. Phys. Lett. 107 (2015) 023903, https://doi.org/10.1063/1.4926971.

[26] H. Kim, H.S. Ahn, H.J. Kwak, M.H. Kim, D.E. Kim, Boiling crisis controlled by capillary pumping and viscous friction: liquid penetration length and dry spot diameter, Appl. Phys. Lett. 109 (2016) 243901, https://doi.org/10.1063/1.4971986.

[27] K.-H. Chu, Y. Soo Joung, R. Enright, C.R. Buie, E.N. Wang, Hierarchically structured surfaces for boiling critical heat flux enhancement, Appl. Phys. Lett. 102 (2013) 151602, https://doi.org/10.1063/1.4801811.
[28] Y. Lee, K. Kim, Y. Kim, D. Kong, J. Park, D. Son, S. Kang, S. Hong, H. Lee, Micro-/Nanohierarchical surfaces for enhanced Pool boiling in large-area silicon multichips, Small Struct. 6 (2025) 2400512, https://doi.org/10.1002/sstr.202400512.
[29] R. Chen, M.-C. Lu, V. Srinivasan, Z. Wang, H.H. Cho, A. Majumdar, Nanowires for enhanced boiling heat transfer, Nano Lett. 9 (2009) 548–553, https://doi.org/10.1021/nl8026857.
[30] H.W. Moon, Y.J. Yoon, J.H. Park, B.-S. Myung, D.E. Kim, Dynamic wetting and boiling characteristics on micro-structured and micro/nano hierarchically structured surfaces, Exp. Thermal Fluid Sci. 74 (2016) 19–26, https://doi.org/10.1016/j.expthermflusci.2015.11.019.
[31] H. Zhao, S. Dash, N.S. Dhillon, S. Kim, B. Lettiere, K.K. Varanasi, A.J. Hart, Microstructured ceramic-coated carbon nanotube surfaces for high heat flux Pool boiling, ACS Appl. Nano Mater. 2 (2019) 5538–5545, https://doi.org/10.1021/acsanm.9b01116.
[32] Y. Song, C.D. Díaz-Marín, L. Zhang, H. Cha, Y. Zhao, E.N. Wang, Three-tier hierarchical structures for extreme Pool boiling heat transfer performance, Adv. Mater. 34 (2022) 2200899, https://doi.org/10.1002/adma.202200899.
[33] M.M. Rahman, E. Ölçeroğlu, M. McCarthy, Role of Wickability on the critical heat flux of structured Superhydrophilic surfaces, Langmuir 30 (2014) 11225–11234, https://doi.org/10.1021/la5030923.
[34] M.M. Rahman, J. Pollack, M. McCarthy, Increasing boiling heat transfer using low conductivity materials, Sci. Rep. 5 (2015) 13145, https://doi.org/10.1038/srep13145.
[35] D. Kong, M. Kang, K.Y. Kim, J. Jang, J. Cho, J.B. In, H. Lee, Hierarchically structured laser-induced graphene for enhanced boiling on flexible substrates, ACS Appl. Mater. Interfaces 12 (2020) 37784–37792, https://doi.org/10.1021/acsami.0c11402.
[36] H. Park, S.F. Ahmadi, T.P. Foulkes, J.B. Boreyko, Coalescence-induced jumping bubbles during Pool boiling, Adv. Funct. Mater. 34 (2024) 2312088, https://doi.org/10.1002/adfm.202312088.
[37] L. Zhang, S. Gong, Z. Lu, P. Cheng, E.N. Wang, Boiling crisis due to bubble interactions, Int. J. Heat Mass Transf. 182 (2022) 121904, https://doi.org/10.1016/j.ijheatmasstransfer.2021.121904.
[38] L. Zhang, J.H. Seong, M. Bucci, Percolative scale-free behavior in the boiling crisis, Phys. Rev. Lett. 122 (2019) 134501, https://doi.org/10.1103/PhysRevLett.122.134501.
[39] L. Zhang, C. Wang, G. Su, A. Kossolapov, G. Matana Aguiar, J.H. Seong, F. Chavagnat, B. Phillips, M.M. Rahman, M. Bucci, A unifying criterion of the boiling crisis, Nat. Commun. 14 (2023) 2321, https://doi.org/10.1038/s41467-023-37899-7.
[40] J. Cho, D. Francis, D.H. Altman, M. Asheghi, K.E. Goodson, Phonon conduction in GaN-diamond composite substrates, J. Appl. Phys. 121 (2017) 055105, https://doi.org/10.1063/1.4975468.
[41] Z. Cheng, V.D. Wheeler, T. Bai, J. Shi, M.J. Tadjer, T. Feygelson, K.D. Hobart, M. S. Goorsky, S. Graham, Integration of polycrystalline Ga_2O_3 on diamond for thermal management, Appl. Phys. Lett. 116 (2020) 062105, https://doi.org/10.1063/1.5125637.
[42] W.-W. Shen, K.-N. Chen, Three-dimensional integrated circuit (3D IC) key technology: through-silicon via (TSV), Nanoscale Res. Lett. 12 (2017) 56, https://doi.org/10.1186/s11671-017-1831-4.
[43] A.V. Golovanov, V.S. Bormashov, N.V. Luparev, S.A. Tarelkin, S.Y. Troschiev, S. G. Buga, V.D. Blank, Diamond microstructuring by deep anisotropic reactive ion etching, Phys. Status Solidi A 215 (2018) 1800273, https://doi.org/10.1002/pssa.201800273.
[44] I. Kano, Pool boiling enhancement by electrohydrodynamic force and diamond coated surfaces, J. Heat Transf. 137 (2015), https://doi.org/10.1115/1.4030217.
[45] R.J. MacNamara, T.L. Lupton, R. Lupoi, A.J. Robinson, Enhanced nucleate pool boiling on copper-diamond textured surfaces, Appl. Therm. Eng. 162 (2019) 114145, https://doi.org/10.1016/j.applthermaleng.2019.114145.
[46] Z. Lv, Y. An, C. Huang, Enhanced pool boiling heat transfer by adding metalized diamond in copper porous materials, Appl. Therm. Eng. 226 (2023) 120288, https://doi.org/10.1016/j.applthermaleng.2023.120288.
[47] S. Torii, Y. Nakamura, S. Tanaka, Boiling heat transfer study of Micro-diamond coated surface using underwater explosion shock wave method, Mater. Today Proc. (2023), https://doi.org/10.1016/j.matpr.2023.04.463.
[48] T. Liu, D. Raabe, W. Mao, S. Zaefferer, Microtexture and grain boundaries in freestanding CVD diamond films: growth and twinning mechanisms, Adv. Funct. Mater. 19 (2009) 3880–3891, https://doi.org/10.1002/adfm.200901231.
[49] A. Zolotukhin, P.G. Kopylov, R.R. Ismagilov, A.N. Obraztsov, Thermal oxidation of CVD diamond, Diam. Relat. Mater. 19 (2010) 1007–1011, https://doi.org/10.1016/j.diamond.2010.03.005.
[50] X. Pei, S. Cheng, Y. Ma, D. Wu, J. Liu, Q. Wang, Y. Yang, H. Li, Structure and wettability property of the growth and nucleation surfaces of thermally treated freestanding CVD diamond films, Appl. Surf. Sci. 346 (2015) 189–193, https://doi.org/10.1016/j.apsusc.2015.03.172.
[51] J.C. Godinez, H. Cho, D. Fadda, J. Lee, S.J. Park, S.M. You, Effects of materials and microstructures on pool boiling of saturated water from metallic surfaces, Int. J. Therm. Sci. 165 (2021) 106929, https://doi.org/10.1016/j.ijthermalsci.2021.106929.
[52] S.G. Kandlikar, A theoretical model to predict Pool boiling CHF incorporating effects of contact angle and orientation, J. Heat Transf. 123 (2001) 1071–1079, https://doi.org/10.1115/1.1409265.
[53] N. Zuber, Hydrodynamic Aspects of Boiling Heat Transfer, United States Atomic Energy Commission, Technical Information Service, 1959.
[54] B.B. Mikic, W.M. Rohsenow, A new correlation of Pool-boiling data including the effect of heating surface characteristics, J. Heat Transf. 91 (1969) 245–250, https://doi.org/10.1115/1.3580136.
[55] A. Zou, D.P. Singh, S.C. Maroo, Early evaporation of microlayer for boiling heat transfer enhancement, Langmuir 32 (2016) 10808–10814, https://doi.org/10.1021/acs.langmuir.6b02642.